Networks from α,ω-Dihydroxypoly(dimethylsiloxane) and (Tridecafluoro-1,1,2,2-tetrahydrooctyl)triethoxysilane: Surface Microstructures and Surface Characterization

Erika Johnston,[†,‡] Steve Bullock,[†,§] Janelle Uilk,[†,§] Paul Gatenholm,[⊥] and Kenneth J. Wynne*[,†,#]

Naval Research Laboratory, Materials Chemistry Branch, Code 6120, Washington, D.C. 20375; Virginia Polytechnic Institute, Chemistry Department, Blacksburg, Virginia 24061; George Mason University, Fairfax, Virginia 22030; Department of Polymer Technology, Chalmers University of Technology, S-412-96 Göteborg, Sweden; and Physical Sciences Division 331, Office of Naval Research, Arlington, Virginia 22217

Received April 22, 1999; Revised Manuscript Received August 17, 1999

ABSTRACT: The dibutyltin diacetate-catalyzed reaction of (tridecafluoro-1,1,2,2-tetrahydrooctyl)triethoxysilane (FTEOS) with dihydroxy-terminated poly(dimethylsiloxane), $HO(Me_2SiO)_nH$, has been used to prepare surface-modified siloxane networks. Surface characterization of these elastomers was carried out with electron spectroscopy for chemical analysis (ESCA) and optical and atomic force microscopy (AFM). Surface phase separation occurs as a function of FTEOS concentration. For example, FTEOS-6x compositions (where 6x is the initial SiOEt/SiOH ratio) exhibited micron scale "islands" of fluorinated siliceous phase (FSP) surrounded by a siloxane-rich "sea". In FTEOS-12x, the FSP formed a continuous layer on the elastomeric network. Differing dynamic contact angle (DCA) analysis protocols with water as the interrogating fluid showed that water contamination affects force vs distance curve (fdc) data on samples up to FTEOS-10x. Intrinsic wetting behavior is reproduced only with a protocol where clean water is used for each DCA cycle. For FTEOS-12x, an FSP monodomain exists characterized by high θ_{adv} (135−6°) and low θ_{rec} (55−56°), similar to previously reported values for fluoroalkyl side chain polymers. Long-term testing showed that the coatings undergo slow chemical degradation by water, with the rate depending on composition. FTEOS-12x is chemically stable in water due to the continuous FSP overlayer.

Introduction

Poly(dimethylsiloxane)-based elastomers (PDMS) are well-known for biomaterials applications such as soft tissue replacement[1−3] and for marine coatings which are easily cleaned of fouling.[4−6] The factors that contribute to the "noninteractive" nature of PDMS materials include (1) a relatively low surface free energy that minimizes the ability of prospective adherents to bond to the surface via polar interactions and (2) high surface molecular mobility (i.e., low glass transition temperature) that inhibits mechanical locking.[7] A third factor that influences surface behavior is the chemical stability of the PDMS surface in aqueous media. Surface stability is essential for predictable, long-term behavior in water, but relatively few studies document the chemical and physical processes involved in surface degradation.[8−11]

We have been interested in hybrid PDMS systems to simplify the preparation of noninteractive films and coatings. Studies of phase separation in hybrid sol−gel systems have focused principally on bulk morphology and the nature of the siliceous domain within the polymeric networks.[12−16] Since hybrid polymer network studies have focused on improving bulk properties (e.g., mechanical, thermal, optical), less attention has been paid to the effects of phase separation on surface properties. The work of Owen on the introduction of side chain fluoroalkyl functionality into siloxanes demonstrates that the modification of PDMS surface chemistry can be fruitful.[17−19] Everaert et al. plasma-treated silicone elastomers and then functionalized the surface with fluoro-organotrichlorosilane.[20] The resulting fluoro-organo functionalized surfaces showed significantly reduced microbial adhesion compared to the untreated silicone elastomer.

In the present paper, fluoroalkyl functionality is introduced into flexible PDMS networks as a pendent group on the alkoxysilane cross-linking agent. The interesting dependence of surface morphology and chemical stability on composition is described below.

Experimental Section

Sample Preparation. Materials. Dibutyltin diacetate (DBTDA) was purchased from Aldrich (catalog no. 29,089-0, CAS[1067-33-0]). Dihydroxy-terminated poly(dimethylsiloxane), $HO(Me_2SiO)_nH$ (26kDa, catalog no. DMS-S31, CAS-[70131-67-8]), (tridecafluoro-1,1,2,2-tetrahydrooctyl)triethoxysilane (FTEOS) (catalog no. SIT8175, CAS[51851-37-7]), and ethyl silicate 40 (ES40) (catalog no. PSI-021, CAS[68412-37-3]) were purchased from Gelest (Tullytown, PA). ES40 consists, according to the manufacturer, of 21% Si.

PDMS (26 kDa) was extracted four times with reagent grade acetone (99+%) followed by one extraction in HPLC grade acetone (99.9+%). Solvent was removed first by vacuum and then by gentle warming and stirring. GPC analysis (vs polystyrene) of the unextracted polymer indicated a number-average molecular weight (M_n) of 18 kDa with a polydispersity, M_w/M_n, of 2.0. GPC of the extracted polymer gave a M_n of 24 kDa, with $M_w/M_n = 1.7$.

Network Formation. The amounts of polymer and alkoxysilane used are indicated in Table 1. The specified amount of polymer was weighed into a 30 mL glass beaker. Alkoxysilane was added dropwise followed by 0.5 wt % dibutyltin diacetate. Stirring commenced immediately using a metal spatula at-

[†] Naval Research Laboratory.
[‡] Virginia Polytechnic Institute.
[§] George Mason University.
[⊥] Chalmers University of Technology.
[#] Office of Naval Research.

10.1021/ma990628y CCC: $18.00
Published on Web 11/05/1999

Table 1. Proportions of 24.4K PMDS and Alkoxysilane Used To Prepare PDMS Sol−Gel Networks

sample ID	alkoxysilane	mass (g) (wt %)	mass (g) (wt %)	ethoxy/ hydroxyl
ES40-1x	ES40	0.09 (0.6)	14.6 (99.0)	1.12
ES40-4x	ES40	0.35 (2.3)	14.6 (97.2)	4.36
FTEOS-2x	FTEOS	0.4 (2.7)	14.6 (96.8)	2
FTEOS-4x	FTEOS	0.8 (5.0)	14.6 (94.5)	3.80
FTEOS-6x	FTEOS	1.3 (8.1)	14.6 (91.4)	6.34
FTEOS-8x	FTEOS	1.6 (9.8)	14.6 (89.7)	7.86
FTEOS-10x	FTEOS	2.1 (12.7)	14.6 (86.9)	10.44
FTEOS-12x	FTEOS	2.5 (14.8)	14.6 (84.7)	12.53

tached to a laboratory motor. Ambient moisture was allowed to drive the hydrolysis reaction. Humidity was not controlled, and the daily relative humidity varied between 20 and 40%. Table 1, column 1, shows the approximate initial SiOEt/SiOH ratio. Thus, the designation "FTEOS-6x" indicates that the amount of FTEOS used in the reaction was approximately 6 times the amount needed to cross-link $HO(Me_2SiO)_nH$. Table 1, column 6, shows that the exact ratio was 6.34.

Cure Kinetics. When the material thickened sufficiently, the mass of material remaining in the beaker and on the spatula was measured in order to calculate the mass of ethanol lost due to hydrolysis. A 2 g sample of material was then measured into a 50 mm diameter polystyrene Petri dish and tilted to fill the dish with a uniform ~2 mm thick layer that subsequently gelled. The dish and evolving network were weighed frequently during 10 days until mass loss plateaued. Calculated mass loss was determined according to eqs 3 and 4 (see later).

Film Preparation. Films for all other analyses were prepared by dipping glass coverslips (Corning, $24 \times 40 \times 1^1/_2$ mm) and distributing the material evenly over both surfaces using a second coverslip as a spatula. Samples were stored vertically in lidded polypropylene boxes containing an open dish of water to provide ample water for cure. When prepared, all cast films were transparent and shiny.

Material Analysis. ESCA. Surface chemistry of all films was investigated by electron spectroscopy for chemical analysis (ESCA). A Perkin-Elmer PHI 5500 equipped with a Mg Kα X-ray source was used for the ESCA measurements. The sample plane was positioned at 20°, 45°, and 70° with respect to the analyzer, resulting in an information depth of 1−10 nm. Charge neutralization was accomplished by a 4−5 eV electron flood gun. PHI sensitivity factors, specific for this instrument, were used to determine elemental composition. Binding energy shifts were determined by referencing the tallest peak in the C_{1s} spectrum to either 292.0 eV for CF_2 groups or 285.0 eV for hydrocarbon. Peak fitting of the C_{1s} region was performed assuming 100% Gaussian peaks.

To ensure that the X-ray radiation during ESCA analysis did not cause degradation of film surfaces, selected samples were investigated several times at the same spot. The atomic ratio of surfaces was not affected by repeated analysis.

AFM and Light Microscopic Imaging. Phase contrast micrographs were taken with a Zeiss Axiotech light microscope fitted with a 50× objective and a Polaroid camera. AFM topographic, Tapping Mode (TM), and phase contrast imaging were performed by advanced surface microscopy (ASM), Indianapolis, IN. Specimens were examined using a Digital Instruments Nanoscope III atomic force microscope fitted with a Nanoscope IIIA tapping mode head and an electronics extender. The samples were scanned with standard silicon tips. An ion source was used to discharge static buildup on sample surfaces. Recently, the AFM data were independently confirmed on a Digital Instruments Nanoscope IIIA at NRL.

TOF-SIMS. Time-of-flight static secondary ion mass spectrometry (TOF-SIMS) was performed on a Physical Electronics model 7200 TOF-SIMS time-of-flight instrument with an 8 keV pulsed Cs^+ primary ion beam with a current of 1.5 pA, a pulse width of 1.2 ns, and a repetition rate of 5000 Hz. A spot size of 100 μm × 100 μm was sampled. The primary ion dose was less than 10^{13} counts/cm^2 in order to maintain static sampling conditions. TOF-SIMS negative ion imaging was performed by raster scanning a 50 μm × 50 μm region with 40 ns pulses. The mass corresponding to F^- was monitored to image fluoropolymer-rich surface regions.

Dynamic Contact Angle (DCA). Advancing and receding contact angles were determined by the Wilhelmy plate method with a Cahn (Cerritos, CA) DCA-312 contact angle analyzer. Measurements were performed in base-bath cleaned, Nanopure water rinsed, 50 mL glass beakers with 17 MΩ Nanopure water as the probe liquid. The accuracy of the measurements was ±1°.

Two protocols were used in the DCA analysis. The first protocol consisted of four force vs distance cycles with a ~1.2 cm travel distance with 10 s dwell times before either sample immersion or withdrawal. Travel speed for these measurements was 100 μm/s. The second protocol recorded five force vs distance cycles with a travel speed of 100 μm/s and dwell times of 10 or 20 s between sample immersion and withdrawal. Ten second dwell times between the immersions and withdrawals were used for cycles 3 and 4. During the 20 s dwell times between immersion and withdrawal for cycles 1, 2, and 5 the beaker and water used for the previous force vs distance curve was removed and replaced by a clean beaker and water.

Mass Loss during Long-Term Water Exposure. Long-term water aging studies were performed on samples cured for at least 1 month. Three replicate samples were stored in Nanopure water containing 200 ppm sodium azide.[21,22] Each week samples were removed, dried for 1 h, and weighed. Initial film masses were calculated by subtracting the average mass of a glass coverslip from the mass of each sample.

Results and Discussion

Network Preparation. This work was initiated to investigate the fluoroalkyl(alkoxy)silane, $CF_3(CF_2)_5(CH_2)_2Si(OC_2H_5)_3$, as a cross-linker and siliceous phase precursor that would impart fluoroalkyl functionality to the siliceous domain of a PDMS network. ES40 was chosen to cross-link $HO(Me_2SiO)_nH$ into fluorocarbon-free controls. It has been shown previously that ES40, a mixture of linear and cyclic oligoalkoxysiloxanes with the approximate stoichiometry $[SiO(OC_2H_5)_2]_n$, is a useful, relatively nonvolatile siliceous phase precursor.[23,24]

Equations 1−4 show in a summarized form the net reactions of $HO(Me_2SiO)_nH$ with ES40 and FTEOS. Initially the reactants are miscible. After addition of DBTDA catalyst, $HO(Me_2SiO)_nH$ and exogenous water from the environment effect the generation of EtOH from Si−OEt groups. Co-condensation of alkoxysilane and hydroxysilane moieties with $HO(Me_2SiO)_nH$ constructs the polymeric network. Self-condensation of hydroxysilane and alkoxysilane moieties gives the siliceous phase.

Figure 1 illustrates a polymer network cross-linked by the fluorinated siliceous phase (FSP). Factors that affect the number of $CF_3(CF_2)_5(CH_2)_2Si(O-)_3$ units incorporated at each cross-linking site include (1) the initial stoichiometry, (2) the relative reaction rates of co-condensation and self-condensation of the alkoxysilane and hydrolyzed alkoxysilane, and (3) the extent of

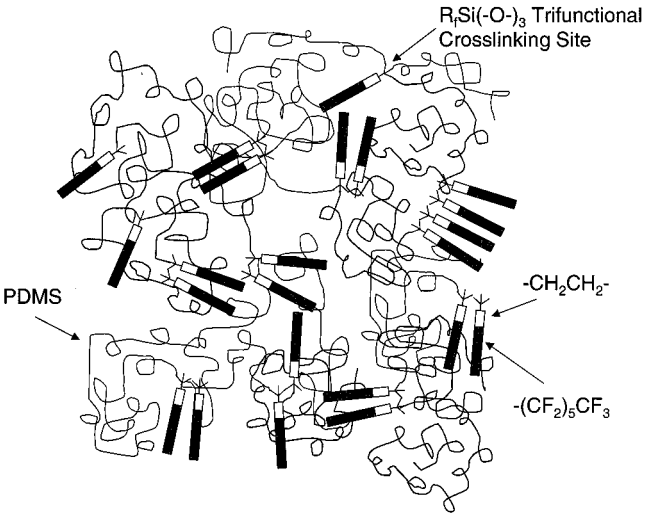

Figure 1. Schematic of polymer network cross-linked by FSP.

phase separation (discussed below). As network formation proceeds, the material undergoes a dynamic change from a sol to a gel, forming a tack-free elastomer within 24 h.

With the compositions investigated herein, cure is not observed in a dry atmosphere; exogenous water is required. Network formation occurs over wide ranges of stoichiometry, as alkoxysilane in excess of that required for condensation with $HO(Me_2SiO)_nH$ undergoes self-condensation (eqs 3 and 4) to produce a siliceous domain.

Eq 1. Network formation by ES40 (DBTDA catalyst)

$$SiO_{2-p/2}(OEt)_p + pH_2O \rightarrow SiO_{2-p/2}(OH)_p + pEtOH \quad (1a)$$

$$SiO_{2-p/2}(OH)_p + (p/2)HO[Me_2SiO]_nMe_2SiOH \rightarrow SiO_{2-p/2}-[O[Me_2SiO]_nMe_2SiO-]_{p/2} + pH_2O \quad (1b)$$

Eq 2. Network formation by FTEOS (DBTDA catalyst)

$$CF_3-(CF_2)_5-(CH_2)_2-Si(OEt)_3 + 3H_2O \rightarrow CF_3-(CF_2)_5-(CH_2)_2-Si(OH)_3 + 3EtOH \quad (2a)$$

$$CF_3(CF_2)_5(CH_2)_2Si(OH)_3 + {}^3/_2HO(Me_2SiO)_nMe_2SiOH \rightarrow CF_3(CF_2)_5(CH_2)_2Si[-O(Me_2SiO)_nMe_2SiO-]_{3/2} + 3H_2O \quad (2b)$$

Eq 3. Self-condensation of excess ES40 (DBTDA catalyst)

$$SiO_{2-p/2}(OEt)_p + (p/2)H_2O \rightarrow SiO_2 + pEtOH \quad (3)$$

Eq 4. Self-condensation of excess FTEOS (DBTDA catalyst)

$$CF_3(CF_2)_5(CH_2)_2Si(OEt)_3 + {}^3/_2H_2O \rightarrow CF_3(CF_2)_5(CH_2)_2SiO_{3/2} + 3EtOH \quad (4)$$

Equations 3 and 4 show that $^1/_2$ mol of oxygen is incorporated into the network for each mole of water utilized in hydrolysis. This was taken into account to calculate the expected mass loss in the cure kinetics study.

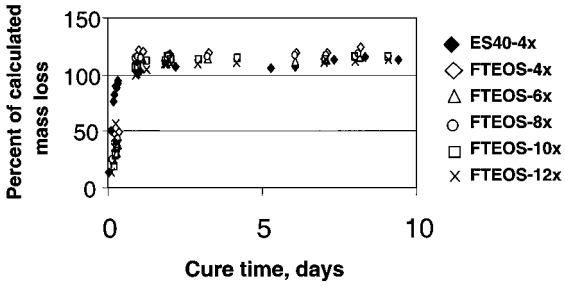

Figure 2. Kinetics of cure.

It was noted above that in a composition such as "FTEOS-6x" the "6" denotes the initial SiOEt/SiOH ratio. The mass of $CF_3(CF_2)_5(CH_2)_2Si(OEt)_3$ and $HO(Me_2SiO)_nH$ determines the stoichiometry of the film or coating because the alkoxysilane is not volatile under these conditions. This approach also works for ES40, although ^{29}Si analysis shows the presence of about 10% $Si(OEt)_4$ (TEOS). TEOS is a volatile alkoxysilane, and the stoichiometry of films and coatings made with TEOS alone cannot be estimated by measuring quantities of reactants.[23]

The siliceous phase in the above equations is represented as being fully dehydrated, but the ratio of Si−O to Si−OH groups is not known. In related work utilizing $MeSi(OEt)_3$, ^{29}Si NMR spectroscopy showed the presence of multiple peaks in the $MeSiO_{1.5}$/MeSiOH (T^2, T^3) region.[23] Siliceous phases for both ES40 and FTEOS compositions very likely contain uncondensed Si−OH groups.

Cure Kinetics. The rates of cure were monitored by measuring mass loss of 50 mm diameter disks for a period of days after film preparation. Observed mass loss as a percent of the expected mass loss is expressed in Figure 2. Time zero corresponds to the moment that catalyst was added to the mixture of macromonomer and alkoxysilane, and stirring was commenced.

The expected mass loss was calculated by summing mass loss occurring during network formation according to eqs 1−4. Figure 2 shows that mass loss is rapid for the first 24 h during which gelation and tack-free film formation occurs. Mass loss then plateaus between 24 and 48 h. By this time, the surface features described in the following section have formed. Figure 2 also shows that the measured mass loss in every case exceeds that calculated by 5−15%. The odor of acetic acid is noticeable during cure, indicating that acetic acid generated by hydrolysis of the catalyst contributes to mass loss.

Equations 2 and 4 show that the hydrolysis reaction requires the diffusion of atmospheric moisture into the evolving network and the diffusion and evolution of ethanol. Network formation requires the diffusion of water and/or ethanol from the evolving network. The permeation rates of ethanol and water through PDMS are relatively high.[25] While the diffusion of small molecules is relatively rapid, the diffusion of macromolecular species is impeded by viscosity buildup in the evolving network. Thus, mass loss as a function of time only provides assurance that hydrolysis is complete when tack-free films are obtained (1−2 days). It is interesting that long-term diffusion processes lead to readily discernible coarsening of surface morphology (vida infra).

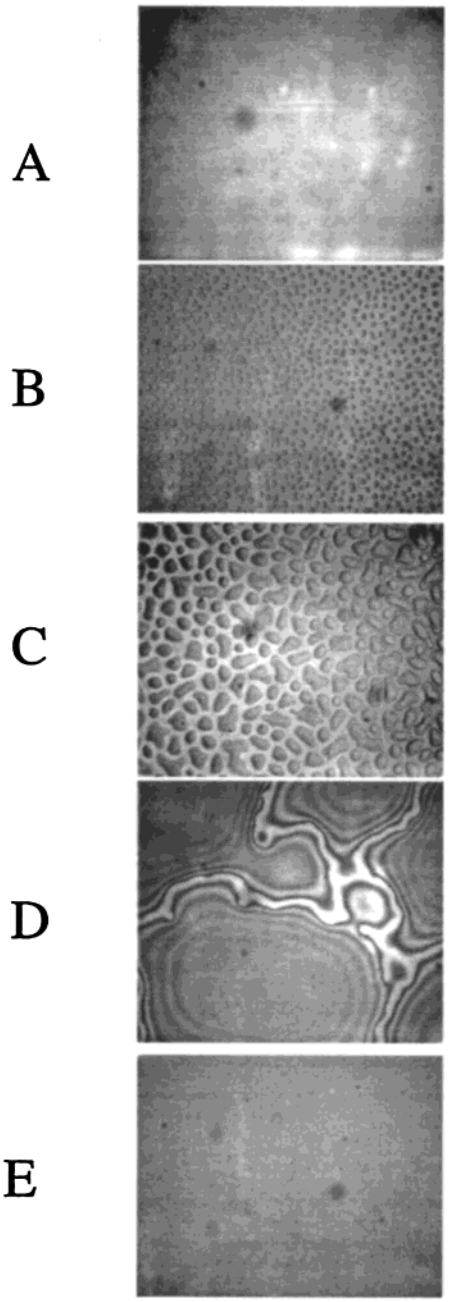

Figure 3. Phase contrast light micrographs: (A) FTEOS-4x, (B) FTEOS-6x, (C) FTEOS-8x, (D) FTEOS-10x, and (E) FTEOS-12x films. Image size is 178 μm × 228 μm.

Visual and Microscopic Observation. After 1−2 days cure, FTEOS-4x films coated on glass slides appear transparent, shiny, and featureless to the eye. Viewed under light microscopy FTEOS-4x materials are featureless, but scattered spots are visible (Figure 3A). FTEOS-6x and -8x films are transparent and shiny 1−2 mm from the sample edges but cloudy and dull across the sample center. A light micrograph of the FTEOS-6x and FTEOS-8x materials (Figure 3B,C) indicates that the dull surface finish is due to light scattering by islands distributed across the film surface.

The overall finish of the FTEOS-10x material is slightly less dull than FTEOS-6x and -8x films, but 0.5 mm diameter bumps are distributed across the surface ~1−2 mm apart. The shiny border is absent on FTEOS-10x. Similar widely dispersed bumps are observed on FTEOS-12x films, but the overall finish is smooth and shiny with a colored refraction pattern. The regions of FTEOS-10x and -12x imaged by light microscopy (Figure 3, D and E, respectively) are representative of the surface between the bumps. Under the microscope, FTEOS-10x surfaces consist of smooth regions separated by narrow, irregular borders while FTEOS-12x coatings are featureless. Both bulk FTEOS-10x and FTEOS-12x films are translucent with a faint bluish haze.

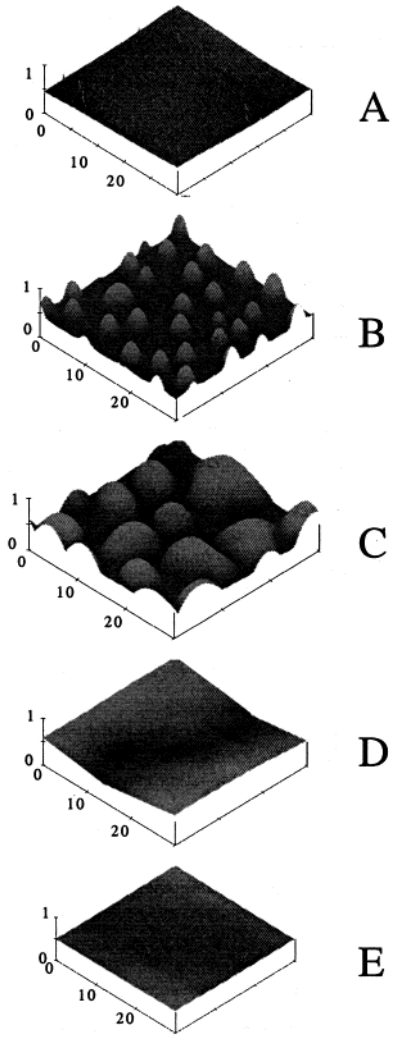

Figure 4. AFM tapping mode images of (A) FTEOS-4x, (B) FTEOS-6x, (C) FTEOS-8x, (D) FTEOS-10x, and (E) FTEOS-12x films. Image area is 30 μm × 30 μm; height is 1 μm.

Atomic Force Microscopy (AFM). To better visualize the surface topography, AFM tapping mode imaging was performed. AFM images (30 μm^2) are presented in Figure 4A−E. FTEOS-4x films are smooth except for a few submicron spots raised above the sample plane (Figure 4A). In the image of FTEOS-6x film, Figure 4B, a pattern of islands about 3 μm in diameter is observed, ranging in height from 210 to 370 nm. The material separating the islands appears slightly rough, perhaps because it is soft and easily deformed by the cantilever interrogations. In the FTEOS-8x image (Figure 4C), the islands are larger and more of them are oblong, as if pairs of proximal islands have merged. Most islands approach 0.5 μm in height and again, the material separating the islands appears to be rougher than the islands themselves. In Figure 4D (FTEOS-10x) the profile of an irregular ravine separating crowded hills is clearly visible, and finally, in the FTEOS-12x image

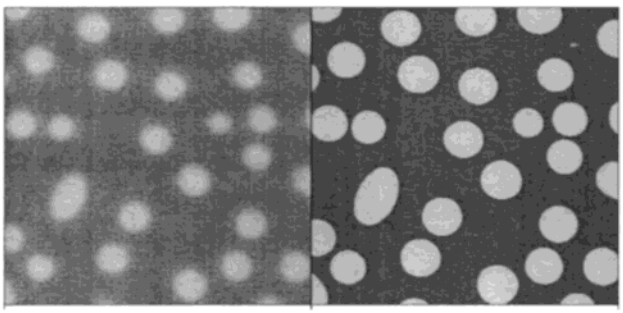

Figure 5. AFM (A) topographical imaging and (B) phase contrast imaging of FTEOS-6x material. In (A), lighter regions correspond to taller features. In (B), lighter regions correspond to regions with higher modulus.

(Figure 4E), the surface is uniform and no significant features are observed.

For composite surfaces, phase imaging AFM enables visualization and classification of different materials.[26] AFM topographic phase imaging of an FTEOS-6x film is shown in Figure 5A,B. The phase offset range is 0°–25°. The phase image is unusual in having only two phase levels, each with a narrow phase range. The islands were about 13.5° higher in phase than the surrounding material. The sharp delineation of the islands seen in the high contrast between the islands and the surrounding PDMS-rich phase provides evidence that the fluoro-organo siliceous phase (FSP) has a higher modulus than the surrounding PDMS-rich "sea".

Flory–Huggins theory of polymer miscibility predicts that polymeric mixtures become less miscible as the molecular weight of the components increases.[27] Flory–Huggins theory assumes nonreactive systems, but it is expected that as the polymeric sol increases in molecular weight toward becoming a gel, the entropy of mixing becomes more negative, thus decreasing the miscibility of the system. Chan and Rey have modeled polymerization-induced phase separation (PIPS) utilizing nonlinear Cahn–Hilliard and Flory–Huggins theories for spinodal decomposition.[28] Their model system consisted of a self-condensing trifunctional monomer. Upon polymerization phase separation of a "solvent" occurs, as in the preparation of a polymer dispersed with liquid crystals.[29] The PIPS system considered by Chan and Rey is simpler chemically than $HO(Me_2SiO)_nH$/FTEOS. The unpolymerized state is similar; as FTEOS and $HO(Me_2SiO)_nH$ are miscible, the enthalpy of mixing (ΔH_{mix}) of two components is positive. The self-condensation of trifunctional FTEOS to form the FSP ultimately drives phase separation in a way similar to the polymerization of the trifunctional monomer of Chan and Rey. However, for FTEOS/$HO(Me_2SiO)_nH$ the phase separation process is impeded as FTEOS undergoes condensation with $HO(Me_2SiO)_nH$. The frustration of phase separation for the $(Me_2SiO)_n$/FSP coatings accounts for their optical transparency, but the low surface free energy of the FSP leads to the surface phase separation noted above.

Some qualitative observations were made about the mechanical robustness of the phase-separated features. Surfaces are usually damaged by rubbing a fingernail across the coated glass slide. The FTEOS-12x surfaces are more resistant to damage than coatings with "islands". However, FTEOS-6x islands were not deformed or damaged by a TM AFM experiment done at a rather low set point ratio (0.2), i.e., hard tapping.

Table 2. Comparison of Elemental Compositions of ES40-4x and FTEOS-4x Materials, As Determined by ESCA, to Calculated Bulk Compositions[a]

element	ES40-4x calcd	ES40-4x, TOA 70	FTEOS-4x calcd	FTEOS-4x, TOA 70	FTEOS-4x, TOA 20
C	49.6	49.5	49.5	49.8	47.7
O	25.4	25.5	24.2	24.3	26.7
Si	25.0	24.8	24.4	23.9	21.3
F		0.0	1.9	1.9	3.9
Sn	0.03	0.2	0.02	0.0	0.4

[a] All units are in atomic percent. TOA is the takeoff angle relative to the plane of the surface.

Table 3. Calculated Percent Elemental Compositions of FTEOS-12x Films Assuming (A) Homogeneous Dispersion of PDMS, FSP, and DBTDA Catalyst and (B) Complete Exclusion of PDMS from the FSP Layer; Columns C–E Show the Measured Elemental Compositions at Three Takeoff Angles (TOAs) Relative to the Plane of the Surface

element	(A) PDMS/FSP	(B) FSP	(C) 20°	(D) 45°	(E) 70°
C	49.5	35.1	33.9	35.7	34.3
Si	24.2	4.1	4.7	4.4	5.9
O	24.4	6.9	7.1	7.2	8.8
F	1.9	53.7	53.7	52.2	50.3
Sn	0.02	0.2	0.6	0.5	0.7

Electron Spectroscopy for Chemical Analysis. Table 2 shows the elemental compositions of ES40-4x and FTEOS-4x films. Elemental composition of the ES40-4x film by ESCA at a TOA of 70° is close to that calculated for PDMS polymer (50% C, 25% O, 25% Si).[30] The presence of tin indicates that there is a trace of catalyst in the outermost 10 nm of ES40-4x (and FTEOS-4x) films. The tin signal increased with time as the sample remained in the UHV environment of the ESCA chamber. Therefore, the appearance of tin in the surface layer (10 nm) may not reflect the amount of catalyst at the surface under normal atmospheric conditions.

Carbon, oxygen, and silicon contents of FTEOS-4x are similar to those for ES40-4x, except for the presence of 2–4% fluorine. The measured FTEOS-4x elemental compositions closely match those calculated from eq 2, with the assumption that all ethoxy groups hydrolyze, all $HO(Me_2SiO)_nH$ hydroxyl groups condense with FTEOS, and all excess FTEOS hydroxyl groups self-condense. At a glancing takeoff angle (TOA) (20°) the measured fluorine concentration (3.9%) of FTEOS-4x films is about double that at 70° (1.9%). The calculated bulk F concentration for FTEOS-4x is 1.9%. Thus, there is some enrichment of FSP at the outermost surface of FTEOS-4x coatings. Optical microscopy gives no evidence of phase separation, and there is only a faint indication of surface phase separation from AFM. The FTEOS-4x composition therefore contains the highest FSP fraction without significant μm-scale surface phase separation.

Table 3 compares the elemental compositions of FTEOS-12x films measured by ESCA with those calculated from the elemental compositions of the precursor materials. Values were calculated assuming (A) that PDMS and $CF_3(CF_2)_5(CH_2)_2SiO_{1.5}$ (FSP) were dispersed homogeneously throughout the film and (B) that the FSP comprised the surface layer. The measured percent F in the FTEOS-12x films closely matches that of $CF_3(CF_2)_5(CH_2)_2SiO_{1.5}$ and indicates complete surface phase

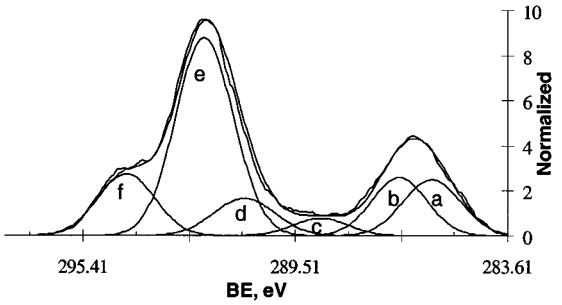

Figure 6. ESCA C_{1s} spectrum of FTEOS-12x: (a) Si***C***H_2, (b) unknown, (c) ***C***H_2CF_2, (d) CH_2***C***F_2, (e) (***C***$F_2)_4$, (f) ***C***F_3.

separation of the FSP. A slight increase in silicon and oxygen is detected at the 70° TOA, indicating the presence of PDMS at greater sampling depth.

An FTEOS-12x C_{1s} spectrum taken at a 20° takeoff angle is shown in Figure 6. The peak assignments provided in Table 4 are consistent with literature values.[45] The peak areas are close to the calculated 1:1:1:4:1 ratio for Si***C***H_2, ***C***H_2CF_2, CH_2***C***F_2, (***C***$F_2)_4$, and ***C***F_3 carbons, respectively. The individual values for CH_2***C***F_2 and (***C***$F_2)_4$ differ slightly from the predicted amounts, perhaps due to small errors in fitting the width of the (***C***$F_2)_4$ peak. A peak is observed at 288.5−288.8 eV and is assigned to the carboxyl carbon of the acetate moiety of the catalyst. This assignment is supported by the similar trend in O═C−O peak area and the measured tin composition (Table 3).

Time-of-Flight Secondary Ion Mass Spectrometry. TOF-SIMS spectra were taken on a PDMS network reference (ES40-1x), a fluoroalkylsilane cross-linked PDMS network that lacked evidence of microscale surface phase separation (FTEOS-2x), and FTEOS-12x which exhibits complete phase separation of the FSP. The ES40-1x control yields peaks at 27.976^+, 43.001^+, and 73.059^+ *m/z*, assigned to Si, Si−CH_3, and {[$(CH_3)_2$-SiO] − 1}, respectively. At higher masses, peaks appear at 147.090^+, 177.002^+, and 191.028^+ *m/z*, all of which are indicative of PDMS.[31]

In the spectra of FTEOS-2x films, evidence of FSP is slight, appearing only as a modest F^- peak at 18.994 *m/z* in the negative ion spectra. Aside from the fluorine anion peak, the positive and negative TOF-SIMS spectra resemble that of the ES40 PDMS control.

Fragments due to FSP predominate in the FTEOS-12x positive ion TOF-SIMS spectra. Fluoroalkyl content is manifested as ($CH_2CH_2CF_2$ − 1) at 77.028^+ and relatively strong peaks at 68.992^+ and 118.992^+ assigned to CF_3 and CF_2CF_3, respectively.[32] A peak corresponding to Si−F is present at 46.975^+ due to rearrangement processes occurring during fragmentation and ionization in the sample selvage. The only evidence of PDMS in FTEOS-12x materials is a minor peak at 73.048^+ corresponding to {[$(CH_3)_2$SiO] − 1}. There are no peaks corresponding to Si−CH_3 or PDMS fragments of molecular weight greater than 100 Da. The presence of catalyst in FTEOS-12x surfaces manifests itself as Sn at 117.032^+ and 118.69^+ and butyl fragments at 57.07^+, 43.055^+, and 29.039^+. These peaks are absent in the ES40-1x and FTEOS-2x materials.

TOF-SIMS imaging of the F^- signal was performed to discriminate between fluoroalkyl-rich and fluoroalkyl-poor regions of FTEOS-6x (Figure 7). The lighter regions in Figure 7 indicate fluoroalkyl-rich regions as streaks. The size of the streaks is of the same order of magnitude as the islands in the AFM image (Figure 4B), but the streaks differ in shape. This suggests that there are gradients in FSP concentration within the outermost surface of the PDMS/FSP network. The reason for the orientation preference of the fluoroalkyl-rich regions is not clear; perhaps this is related to the vertical position of the samples during dipping and curing.

Dynamic Contact Angle Analysis. Dynamic contact angle measurements (DCA) were performed by the Wilhelmy plate technique, whereby the net force acting on a sample is measured as the sample is immersed and withdrawn from an interrogation liquid. The force balance acting on a sample during immersion and withdrawal can be described by eqs 5 and 6:

$$F_{\text{net}} = F_{\text{surface tension}} + F_{\text{gravity}} - F_{\text{buoyant}} \quad (5)$$

$$F_{\text{net}} = \sigma_{\text{LV}} P \cos\theta_{\text{d}} + mg - (\rho_{\text{L}} - \rho_{\text{S}}) gPh \quad (6)$$

where F_{net} is the net force acting on the sample, σ_{LV} is the liquid/vapor surface tension, θ_{d} is the dynamic contact angle, P is the sample perimeter, m is the sample mass, g is the gravitational constant, ρ_{L} and ρ_{S} are the liquid and sample densities, respectively, and h is the distance that the sample is immersed in the interrogation liquid. By taring out the sample mass and extrapolating the force vs distance curve (fdc) to the point of zero immersion ($h = 0$), the last two terms in eq 6 are eliminated, and the equation can be rearranged to calculate the dynamic contact angle:

$$\theta_{\text{d}} = \arccos(F_{\text{net}}/\sigma_{\text{LV}} P) \quad (7)$$

where θ_{d} is the advancing contact angle (θ_{adv}) during immersion and the receding contact angle (θ_{rec}) during sample withdrawal. At the stage speed employed, each fdc takes about 1.5 min, and there is a 10 s submerged dwell time. The total time per cycle is about 3 min.

For flame-treated glass, which is used to check the surface tension of water, the fdc's superpose during immersion and withdrawal; that is, there is no hysteresis ($\theta_\Delta = \theta_{\text{adv}} - \theta_{\text{rec}} = 0°$), while for siloxane-containing polymers hysteresis is substantial.[7,22,23] The Wilhelmy plate method is particularly attractive for the study of the interaction of fluids such as water with polymer surfaces.[33] Advancing and receding fdc curves allow a clear differentiation between the interaction of a "dry" and "wet" polymer surface. The resulting hysteresis has been attributed to the effects of surface chemical heterogeneity, surface roughness, surface reorganization, and surface hydration on the solid/liquid/vapor interface.[33,34] Hysteresis can also be influenced by the purity of the probe liquid and therefore by dissolution of the sample or leaching of species from the sample. In the following examination of FTEOS-8x, we show how leaching from the sample can affect wettability.

Wetting Behavior of FTEOS-8x. Figure 8 shows DCA data for FTEOS-8x obtained with the two different protocols described in the Experimental Section. Contact angle data from the fdc curves are collected in Table 5. The results for the two protocols are quite different and clarify the origin of the changes in fdc's as a function of time.

The data shown in Figure 8A were obtained from a pristine sample of FTEOS-8x using the same beaker and water for all four cycles. In Figure 8A the first cycle (fdc-a1, fdc-r1) is different from successive cycles. Contact angles are $\theta_{\text{adv},1}$, 117° and $\theta_{\text{rec},1}$, 91°. In the second cycle, fdc-a2 shows nonlinear behavior. Then, fdc-r2 and

Table 4. Comparison of FTEOS-12x C_{1s} Peak Areas Measured at Three Takeoff Angles with Those Calculated for C in the FSP, i.e., for $[CF_3(CF_2)_4CF_2CH_2CH_2SiO_{1.5}]_n$

carbon (***C***)	lit. BE, eV [ref 45]	obsd BE, eV	calc area %	area %, 20°	area %, 45°	area %, 70°
Si***C***H_2CH_2−	284.0−286.6	285.6−0.7	12.5	13.1	13.0	14.6
−***C***H_2−CF_2−	285.6−287.3	286.6−0.7	12.5	13.1	13.6	15.3
O−C═O	288.0−290.0	288.5−0.8		3.9	0.91	5.8
−CH_2***C***F_2−	290.1−291.8	290.4−291.2	12.5	9.2	10.6	7.7
−(***C***F_2)$_4$−	291.8−293.3	292.0	50.0	46.2	48.3	45.0
−***C***F_3	292.6−294.4	294.1−0.2	12.5	14.4	13.6	11.6

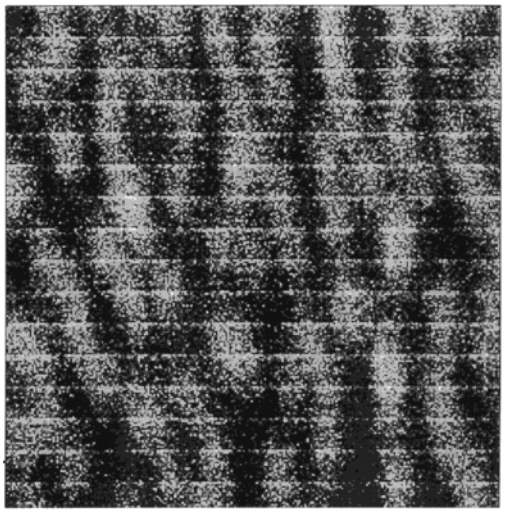

Figure 7. TOF-SIMS image of FTEOS-6x material.

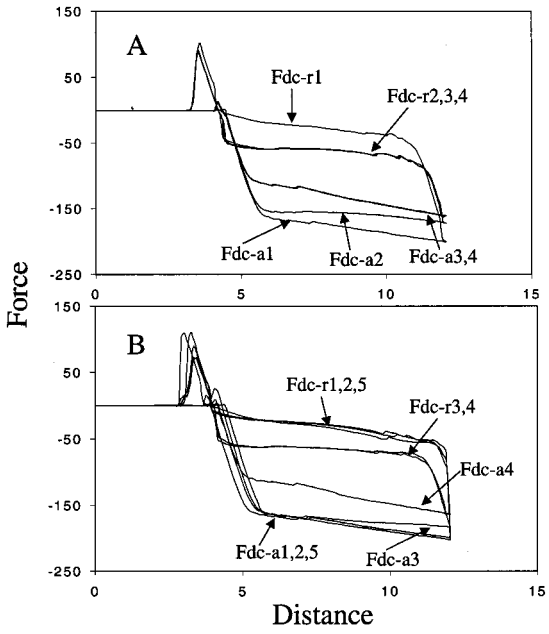

Figure 8. Wetting behavior of FTEOS-8x with two differing DCA protocols: (A) same water used for all four cycles and (B) water and beaker changed before fdc-a1, fdc-a2, and fdc-a5 and fdc-r1, fdc-r2, and fdc-r5.

succeeding receding and advancing fdc's are identical, with θ_{adv} of 106° and θ_{rec} of 98°.

The data in Figure 8B were taken on a pristine sample of FTEOS-8x with a protocol that included changing both the beaker and water before advancing and before receding fdc's at the intervals indicated. The first cycle where clean water was used is identical for both protocols. That is, changing the water for both immersion and withdrawal made no difference in the traces for cycle 1.

Table 5. Contact Angle Data (±1°) for DCA Traces Shown in Figure 8

	Figure 8A protocol		Figure 8B protocol	
cycle	θ_{adv}	θ_{rec}	θ_{adv}	θ_{rec}
1	117	91	118	90
2	*a*	98	116	91
3	106	98	*a*	100
4	106	99	105	99
5			116	91

[a] A nonlinear fdc.

The second cycle (Figure 8B), where clean water was used for fdc-a2 and fdc-r2, is different from the corresponding cycle for unchanged water (Figure 8A). Fdc-a2 and fdc-r2 with clean water for both immersion and withdrawal (Figure 8B) are identical to those for the first cycle. The third cycle shown in Figure 8B was carried out without changing the water. The slope of fdc-a3 matches closely fdc-a2, Figure 8A, although the onset of nonlinearity is later for fdc-a3, Figure 8B. Fdc-r3, Figure 8B, is the same as fdc-r2, Figure 8A. The fourth cycle shown in Figure 8B was also done without a water change. The fdc's observed for the fourth cycle, Figure 8B, are the same as the third cycle, Figure 8A.

Figure 8B shows the result of reintroducing clean water for immersion and withdrawal for the fifth cycle. The fdc's are identical to cycles 1 and 2 that used clean water. The fdc data for the first cycle can be reproduced at any time for FTEOS-8x by using clean water for immersion and withdrawal.

In summary, the first advancing and receding traces measured in clean water are virtually identical, while subsequent traces in "used" water drift to a different set of values. These DCA results are explained by water contamination. Cycles for clean water exhibit advancing and receding fdc's that reflect the interaction of uncontaminated water with the sample surface. Results for FTEOS-8x show that water contamination effects are not observed for the first DCA cycle in clean water. The degradation of the interfacial tension is initiated during the second cycle. We previously attributed changes in wetting behavior shown in Figure 8A to surface reorganization,[8] as suggested by Riddiford for silicone elastomers.[35] We became convinced that water contamination was the cause of the changes described above because of the similarity between traces 3 and 4 in Figure 8A,B and the traces obtained when a pristine sample was tested in previously "used" water.

Wetting Behavior as a Function of Composition. Figure 9 shows advancing and receding fdc's for compositions ranging from FTEOS-4x to FTEOS-12x.[36] On the basis of the above results for FTEOS-8x, clean water was used for the cycle shown, and the water was not changed for the withdrawal process. Table 6 summarizes contact angle data. Despite the obvious difference in topology observed by TM-AFM and optical microscopy, the wetting behavior for the FTEOS-4x, -6x, -8x, and -10x compositions is similar. The observed

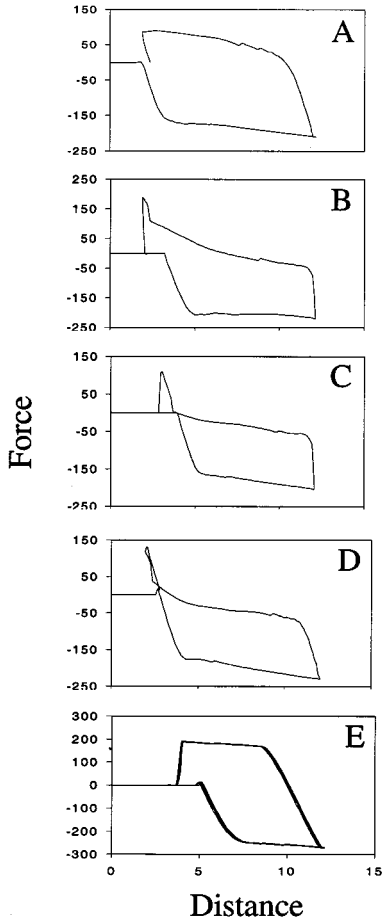

Figure 9. DCA traces for (A) FTEOS-4x, (B) FTEOS-6x, (C) FTEOS-8x, (D) FTEOS-10x, and (E) FTEOS-12x films.

Table 6. Contact Angle Data (±1°) for FTEOS 4−12x

composition	θ_{adv}	θ_{rec}	composition	θ_{adv}	θ_{rec}
4x	117	73	10x	118	92
6x	120	89	12x	135	56
8x	117	91			

advancing contact angles for compositions up to FTEOS-10x are somewhat higher than those for nonfluorinated alkoxysilane-cured samples. Comparable advancing contact angles for ES40-cured samples are about 110°. We are reassessing data for alkoxysilane-cured samples, as water contamination was not taken into account in previous studies.[8,23]

FTEOS-12x. For FTEOS-12x, $\theta_{adv,1}$ and $\theta_{rec,1}$ are identical to those obtained in second and subsequent cycles. Although accurate surface tension data for FTEOS-4x to -10x samples are obtainable without changing water only during the first cycle, FTEOS-12x samples have wetting behavior that is independent of protocol. Surface analytical data presented in prior sections demonstrate that FTEOS-12x has a smooth surface layer of FSP that is compositionally represented by the formula $[CF_3(CF_2)_5(CH_2)_2{-}Si{-}O_{3/2}]_n$.[23,37] Apparently, the FSP monodomain at the surface is more chemically stable than the mixed domain surface. In addition, the surface FSP provides a barrier for the diffusion of sol and/or cyclics and other low molecular weight contaminants originating from the macromonomer.

The high θ_{adv} (135°) and low θ_{rec} (56°) observed for FTEOS-12x have been seen previously for polymers containing fluoroalkyl side chains.[23,38,39] The consistently large θ_Δ (≈80°) is explained by a reversible, short-range interaction between liquid water and the surface that is illustrated in Figure 10A,B. The high θ_{adv} is a result of water advancing over the thermodynamically favored fluorocarbon-like surface generated at the air−polymer interface (Figure 10A). Once the surface is wetted, water hydrogen-bonds to acidic CH_2 groups adjacent to the CF_2 group in the fluorocarbon moiety, and perhaps to near surface Si−OH groups, accounting for the low θ_{rec} (Figure 10B).

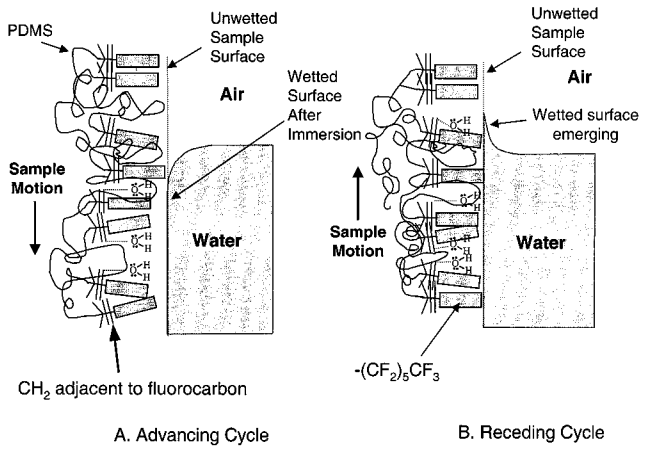

Figure 10. Representation of the surface of FTEOS-12x with a contribution from the FSP: (A) fluorocarbon moiety increases θ_{adv} and (B) hydrogen bonding of H_2O to $C\mathbf{H}_2CF_2$ decreases θ_{rec}.

The proposed amphipathic wettability of FTEOS-12x is analogous to the explanation proposed by Katano,[23] for fluorinated side-chain acrylates. The model is also consistent with the theory of Johnson and Dettre.[40] The latter authors showed theoretically and experimentally that a small surface area fraction of hydrophilic sites on a hydrophobic surface markedly reduces θ_{rec} but had only a slight effect on θ_{adv}. In contrast to compositions of lower FTEOS-content, fdc's for FTEOS-12x films are reproducible after immersion of the films for at least 1 month in water. This is attributed to the chemical stability of these films that is discussed further below.

Chemical and Morphological Stability. A main result of the work reported herein is the generation of thermodynamically driven, compositionally modulated, surface structures. Such structures are of interest, as it is known that geometric patterning of surfaces can influence the settlement and growth of organisms.[41] Before testing biointeractive effects of patterned surfaces, it is imperative that chemical stability be understood. Characterizing chemical stability is one facet of understanding biodurability. Understanding constituent features of biodurability provides a basis for correlating biointeractive effects with surface and bulk structure. If investigating geometric (patterning) effects, for example, one should be certain that results are not confused by polymer surface hydrolysis (erosion).

Mass Loss during Long-Term Water Exposure. To evaluate the stability of the new elastomeric coatings generated by fluorinated alkoxysilane cure, coated slides (cure, 1 month) were immersed in water, and mass loss was monitored as a function of time. The data in Table 7 show that, compared with the ES40-4x control, the FTEOS-4x analogue loses mass 3 times as fast. However, as more FSP is incorporated in the elastomer, the stability of the material to long-term water exposure

Table 7. Mass Loss Rate of Networks Immersed in Water for 7 Weeks

sample ID	wt % loss/week	sample ID	wt % loss/week
ES40-4x	0.34	FTEOS-8x	0.27
FTEOS-4x	1.03	FTEOS-10x	0.14
FTEOS-6x	0.35	FTEOS-12x	0.01

improves. We believe that the FSP overlayer formed on the surface serves as a stabilizing barrier. Further work is underway examining ways of increasing the chemical stability of these systems.

Morphological Stability. TM-AFM images were obtained on an FTEOS-6x sample aged in air for ∼18 months. Surprisingly, a significant coarsening of the surface FSP features was observed compared to the morphology after cure for 2 months. The size of the FSP surface features on the aged FTEOS-6x sample approached those of the FTEOS-8x image shown in Figure 3c.

Light microscopy on an FTEOS-12x sample also aged for 18 months in air showed phase separation on a scale of ∼100 μm. That is, the initial monodomain observed after 2 months cure phase separated after 1 year. This phase separation was reflected in wetting behavior. The stable, high hysteresis observed for the FSP monodomain (Figure 9E) resulting after 2 months cured was replaced with more PDMS-like wetting behavior similar to FTEOS-4x to -10x compositions reported above.

Summary

Phase separation-induced enrichment of one component at the polymer surface has been previously observed in block copolymers[42,43] and polymer blends.[44] In the present work, a PDMS network surface is enriched in a fluorinated siliceous phase (FSP) generated by sol gel chemistry. Negative ion TOF-SIMS detected fluorine (F^-) at the surface in compositions as low as 2.7 wt % FTEOS, barely twice the amount required by stoichiometry to cross-link the $HO(Me_2SiO)_nH$. FTEOS-6x compositions produced micron-sized FSP surface islands, while FTEOS-12x (14.6 wt % FSP) gave a conformal cross-linked FSP overlayer. ESCA data on FTEOS-12x show that the FSP surface domain has a thickness of at least 10 nm. The height of the FSP islands (ca. 0.4 μm) suggests that the FSP surface phase may have a thickness comparable to the height. At present we do not know the extent and nature of bulk phase separation.

Differing DCA protocols with water as the interrogating fluid showed that water contamination affects fdc data on samples up to FTEOS-10x. Intrinsic wetting behavior is reproduced only when clean water is used for each advancing and receding fdc. The observed advancing contact angles for compositions up to FTEOS-10x (∼118°) do not show significant compositional dependence and are somewhat higher than those for nonfluorinated alkoxysilane cure. Comparable advancing contact angles for ES40 cured samples are about 110°.

At the highest FSP composition of FTEOS-12x, essentially a monodomain of FSP exists characterized by high θ_{adv} (135−6°) and low θ_{rec} (55−56°). These data are comparable to previously reported values for fluoroalkyl side chain polymers. FTEOS-12x compositions are chemically stable to mass loss over the time frame of the experiments discussed above. Water contamination is not observed by DCA, and wettability is constant.

Long-term (18 months) aging effects on the morphology and surface wetting behavior of these fluorinated alkoxysilane networks are significant. FSP surface-domain coarsening occurs for compositions less than FTEOS-10x. In contrast, the FSP monodomain observed for FTEOS-12x compositions after 2 months cure phase separates on the 100 μm scale, and surface wetting behavior becomes more PDMS-like.

Acknowledgment. We thank the Strategic Environmental Research and Development Program (SERDP) and the ONR Scientific Officer Research Program (SORP) for partial support of this research. The authors also thank the Surface Analysis Recharge Center (SARC) at the University of Washington for conducting the TOF-SIMS experiments. SARC is funded under NSF Engineering Research Center Grant EEC9529161. P.G. thanks the MASTEC-Programme for support.

References and Notes

(1) Compton, R. *J. Long-Term Effects Med. Implants* **1997**, *7*, 29.
(2) Courtney, J. M.; Lamba, N. M. K.; Sundaram, S.; Forbes, C. D. *Biomaterials* **1994**, *5*−*10*, 737.
(3) Isetta, C.; Merville, C.; Hechema, R.; Philip, P.; Bayle, J.; Briquet, F.; Chevalier, Th.; Sanchez, B.; Jourdan, J. *Br. J. Anaesth.* **1996**, *76*, 16.
(4) Griffith, J. R. US Patent 5,449,553, *Nontoxic antifouling systems*, Sept 12, 1995.
(5) Baier, R. E.; Meyer, A. E. *Biofouling* **1992**, *6*, 165−180.
(6) Alberte, R. S.; Snyder, S.; Zahuranec, B. J.; Whetstone, M. *Biofouling* **1992**, *6*, 91−95.
(7) Pike, J. K.; Ho, T.; Wynne, K. J. *Chem. Mater.* **1996**, *8*, 856−860.
(8) Goodwin, M.; Vu, A.; Bullock, S.; Ervin, A.; Gatenholm, P.; Wynne, K. *Proc. Am. Chem. Soc., Div. Polym. Mater. Sci. Eng.* **1997**, *76*, 91.
(9) Tezuka, Y.; Kazama, H.; Imai, K. *J. Chem. Soc., Faraday Trans.* **1991**, *87*, 147−152.
(10) Kennan, J. J.; Peters, Y. A.; Swarthout, D. E.; Owen, M. J.; Namkanisorn, A.; Chaudhury, M. K. *J. Biomed. Mater. Res.* **1997**, *36*, 487−497.
(11) Batich, C.; DePalma, D.; Marotta, J.; LaTorre, G.; Hardt, N. S. *Curr. Top. Microbiol. Immunol.* **1996**, *210*, 13−23.
(12) Huang, H.-H.; Orler, B.; Wilkes, G. L. *Macromolecules* **1987**, *20*, 1322−1330.
(13) Chujo, Y. *Curr. Opin. Solid State Mater.* **1996**, *1*, 806−811.
(14) Mark, J. E. *Polym. Eng. Sci.* **1996**, *36*, 2905−2920.
(15) Hyeon-Lee, J.; Guo, L.; Beaucage, G.; Macip-Boulis, M. A.; Yang, A. J. M. *J. Polym. Sci., Part B: Polym. Phys.* **1996**, *34*, 3073−3080.
(16) Landry, M. R.; Coltrain, B. K.; Landry, C. J. T.; O'Reilly, J. M. *J. Polym. Sci., Part B: Polym. Phys.* **1995**, *33*, 637−655.
(17) Kobayashi, H.; Owen, M. J. *Trends Polym. Sci.* **1995**, *3*, 330−335.
(18) Owen, M. J. *Ind. Eng. Chem. Prod. Res. Dev.* **1980**, *18*, 97−103.
(19) Owen, M. J.; Kobayashi, H. *Macromol. Symp.* **1994**, *82*, 115−123.
(20) Everaert, E. P. J. M.; van der Mei, H. C.; Busscher, H. J. *Colloids Surf. B: Biosurf.* **1998**, *10*, 179−190.
(21) Hogt, A. H.; Gregonis, D. E.; Andrade, J. D.; Kim, S. W.; Dankert, J.; Feijen, J. *J. Colloid Interface Sci.* **1985**, *106*, 289.
(22) Bullock, S.; Johnston, E. E.; Willson, T.; Gatenholm, P.; Wynne, K. J. *J. Colloid Interface Sci.* **1999**, *210*, 18.
(23) Wynne, K. J.; Ho, T.; Johnston, E.; Myers, S. *Appl. Organomet. Chem.* **1998**, *12*, 763.
(24) Honeychuck, R.; Wynne, K. J. Manuscript in preparation.
(25) Feng, Y.; Honnma, S.; Ito, A. *J. Appl. Polym. Sci.* **1997**, *63*, 433−438.
(26) Maganov, S. N.; Elings, V.; Whangbo, M.-H. *Surf. Sci.* **1997**, *375*, L385−L391.
(27) Flory, P. J. *Principles of Polymer Chemistry*; Cornell University Press: Ithaca, NY, 1953; Chapter XIII.
(28) Chan, P. K.; Rey, A. D. *Macromolecules* **1997**, *30*, 2135−2143.
(29) Doan, J. W.; Vaz, N. A.; Wu, B.-G.; Zumer, S. *Appl. Phys. Lett.* **1986**, *48*, 269.
(30) Duel, L. A.; Owen, M. J. *J. Adhes.* **1983**, *16*, 49.

(31) Newman, J. G.; Hohlt, T. A. *Static SIMS Handbook of Polymer Analysis: A Reference Book of Standard Data for Identification and Interpretation of Static SIMS Data*; Perkin-Elmer Corp., Physical Electronics Division: Eden Prairie, MN, 1991.
(32) Sun, F.; Castner, D. G.; Mao, G.; Wang, W.; McKeown, P.; Grainger, D. W. *J. Am. Chem. Soc.* **1996**, *118*, 1856−1866.
(33) Johnson, R. E., Jr.; Dettre, R. H. In *Wettability*; Surfactant Science Series Vol. 49; Berg, J. C., Ed.; M. Dekker: New York, 1993; Chapter 1, pp 1−73.
(34) Cain, J. B.; Francis, D. W.; Venter, R. D.; Neumann, A. W. *J. Colloid Interface Sci.* **1983**, *94*, 123−130.
(35) Phillips, M. C.; Riddiford, A. C. *J. Colloid Interface Sci.* **1972**, *41*, 77.
(36) A modification of the first protocol described in the Experimental Section was used. Travel speed was 100 μ/s and dwell time was 0 s.
(37) The formula $[CF_3-(CF_2)_5-(CH_2)_2-Si-O_{3/2}]_n$ is used, but with ambient temperature alkoxysilane cure, it is likely that a significant fraction of the SiOH groups formed on hydrolysis do not undergo condensation to form Si−O−Si. ^{29}Si NMR spectroscopy on alkoxysilane (TEOS)-cured PDMS showed that the ratio of [**Si**(−O−)$_3$(−OH)] (T^3) to [**Si**(−O−)$_4$] T^4 Si's was about 1:1.
(38) Katano, Y.; Tomono, H.; Nakajima, T. *Macromolecules* **1994**, *27*, 2342−2344.
(39) Owen, M. J. *Ind. Eng. Chem. Prod. Res. Dev.* **1980**, *19*, 97.
(40) Johnson, R. E., Jr.; Dettre, R. H. *Surface and Colloid Science*; Matijevic, E., Ed.; Wiley-Interscience: New York, 1969; Vol. 2, pp 85−153.
(41) (a) Chehroudi, B.; Gould, T. R.; Brunette, D. M. *J. Biomed. Mater. Res.* **1988**, *22*, 459. (b) von Recum, A. F.; van Kooten, T. G. *J. Biomater. Sci., Polym. Ed.* **1995**, *7*, 181. (c) Britland, S.; Clark, P.; Connolly, P.; Moores, G. *Exp. Cell Res.* **1992**, *198*, 124. (d) Healy, K. E.; Thomas, C. H.; Rezania, A.; Kim, J. E.; McKeown, P. J.; Lom, B.; Hockberger, P. E. *Biomaterials* **1996**, *17*, 195.
(42) Clark, D. T.; Peeling, J.; O'Malley, J. M. *J. Polym. Sci., Polym. Chem.* **1976**, *14*, 543.
(43) Chen, X.; Gardella, J. A., Jr. *Macromolecules* **1994**, *27*, 3363−3369.
(44) Schmitt, R. L.; Gardella, J. A., Jr.; Salvati, L., Jr. *Macromolecules* **1986**, *19*, 648−651.

MA990628Y